Diapirs as the source of the sediment signature in arc lavas

Mark D. Behn[1]*, Peter B. Kelemen[2], Greg Hirth[3], Bradley R. Hacker[4] and Hans-Joachim Massonne[5]

Island arc lavas, erupted above subduction zones, commonly contain a geochemical component derived from partial melting of subducted sediment. It is debated whether this sediment melt signature, with enriched trace element concentrations and isotope ratios, forms at relatively low or high temperatures. Here we compile and analyse the geochemistry of metamorphosed sedimentary rocks that have been exposed to pressures between 2.7 and 5 GPa during subduction at a range of locations worldwide. We find that the trace elements that form the sediment melt signature are retained in the sediments until the rocks have experienced temperatures exceeding 1,050 °C. According to thermal models, these temperatures are much higher than those at the surface of subducted slabs at similar pressures. This implies that the sediment melt signature cannot form at the slab surface. Using instability calculations, we show that subducted sediments detach from the downgoing slab at temperatures of 500–850 °C to form buoyant diapirs. The diapirs rise through the overlying hot mantle wedge, where temperatures exceed 1,050 °C, undergo dehydration melting, and release the trace elements that later form the sediment melt signature in the erupted lavas. We conclude that sediment diapirism may reduce the transport of trace elements and volatiles such as CO_2 into the deep mantle.

Ba, Th, Be, Pb, and light rare-earth elements (REE) are enriched in partial melts of metasediment, but many of these elements are relatively immobile in aqueous fluids[1]. The enrichment of these elements, and their correlation with the flux and composition of subducted sediments, has been interpreted to reflect a 'sediment melt' signature in arc lavas[2–4]. Subduction zone thermal models that incorporate temperature- and stress-dependent viscosity[5–8] produce slab-top temperatures above the fluid-saturated sediment solidus (>600–700 °C at ≤3 GPa; refs 9,10), and H_2O/Ce and H_2O/K ratios in melt inclusions from arc lavas are consistent with fluid fluxed melting of sediments at 750° to more than 950 °C beneath several global subduction systems[11–13]. Alternatively, it has been suggested that subducting sediment detaches as solid-state diapirs, and melts at higher temperatures as it ascends through the mantle wedge[14–17].

The key to distinguishing between these models is determining the conditions under which sediment melting occurs in subduction zones. A major challenge in evaluating these conditions is the difficulty in sampling the residues of sediment melts. Most studies of rocks exhumed from subduction zones focus on either (1) basaltic compositions analogous to subducted oceanic crust or (2) unusual metasediments that attained high temperatures at relatively low peak pressures, different from even the hottest slab-top geotherms. Mafic ultrahigh-pressure (UHP) rocks subducted to pressure–temperature conditions above the fluid-saturated basalt solidus show MORB-like concentrations in fluid-immobile elements[18], such as Th and La. This suggests that either melting was suppressed in these rocks because of low H_2O activity or that minor phases retained Th, La, and other light REE in the solid residue. Similarly, metasediments from Santa Catalina Island[19] show only minor depletion of Th, La, Pb and Sr. However, these samples attained peak pressure–temperature conditions of 600 °C and 1–1.2 GPa, a higher temperature at a given pressure than any steady state subduction geotherm, yet below the fluid-saturated sediment solidus. In another example, high-pressure and UHP metasediments from the western Alps that reached peak temperatures ≤630 °C along a plausible subduction geotherm show little sign of depletion of fluid-immobile elements compared to average shale[20].

Characterizing the conditions of sediment melting

To characterize the residues of sediment melting, we analysed and compiled other data on high- to UHP rocks (peak pressures mostly between 2.7 and 5 GPa; hereafter loosely termed UHP) associated with subduction systems to assess whether these rocks lost Th, Pb, and other fluid-immobile trace elements. To isolate pelitic sediment protoliths from igneous compositions we considered only peraluminous UHP compositions (see Supplementary Information for data sources and the method for identifying UHP metapelites). Comparing these data to a compilation of peraluminous shale compositions representative of the incoming sediment at subduction zones (see Supplementary Information for data sources), we find that UHP metapelites with peak temperatures of 700°–1,050 °C have compositions that lie within the compositional range of shale (Fig. 1a). This indicates that the UHP rocks are indeed representative of peraluminous subducting, pelitic sediments. However, many UHP metapelites that attained temperatures >1,050 °C show depletions in highly incompatible elements, including Th, Sr, Pb, and Nd, as expected for the residues of melting that could result in extensive recycling of the 'sediment component' from subducting metasediments to arc magmas (Fig. 1 and Supplementary Figures). Even among our samples that reached >1,050 °C, some are not depleted, suggesting that yet higher degrees of melting and/or more efficient melt extraction are required to fully exhaust the minor phases that host key trace elements in the solid residue.

[1]Department of Geology and Geophysics, Woods Hole Oceanographic Institution, 360 Woods Hole Road MS #22, Woods Hole, Massachusetts 02543, USA, [2]Lamont Doherty Earth Observatory, Columbia University, Palisades, New York 10964, USA, [3]Department of Geological Sciences, Brown University, Providence, Rhode Island 02912, USA, [4]Department of Earth Science, University of California, Santa Barbara, California 93106, USA, [5]Institut für Mineralogie und Kristallchemie, Universität Stuttgart, D-70174 Stuttgart, Germany. *e-mail: mbehn@whoi.edu.
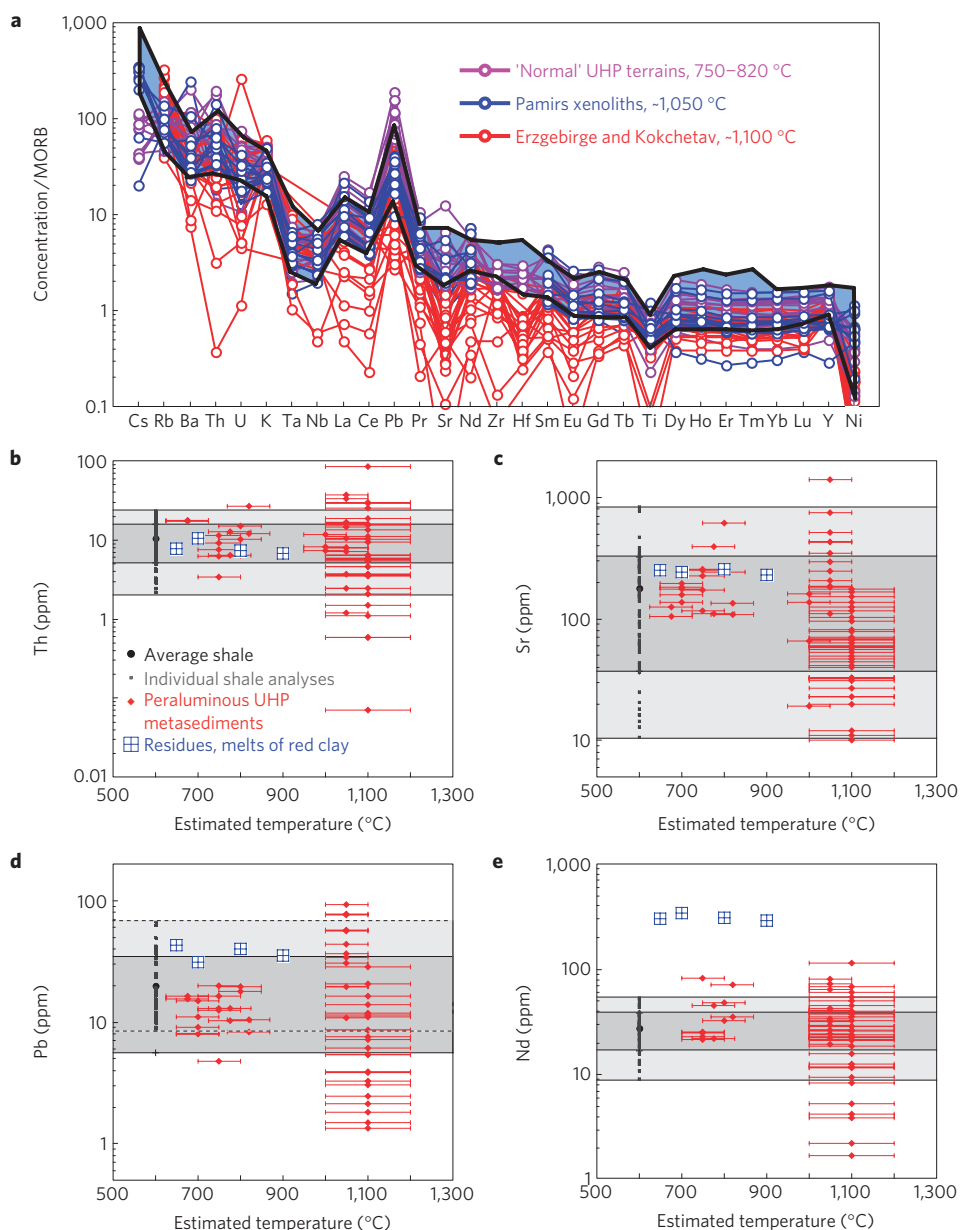
Figure 1 | Comparison of pelitic UHP metasediment compositions to average shale, greywacke and loess compositions. a, Trace element diagram for pelitic UHP metasediments. 1σ envelope for average shale, greywacke, and loess is shown as blue field with black outlines. **b–e**, Trace element concentrations in pelitic UHP metasediments (red diamonds, see Supplementary Information for error estimates) as a function of peak metamorphic temperature compared to our average peraluminous shale and greywacke composition (black circle at arbitrary temperature of 600 °C), our compiled peraluminous shale, greywacke, and loess compositions (small grey squares, full data range denoted by light grey shaded region), and 1σ for our average shale and greywacke composition (dark grey shaded region). Shown for comparison are compositions of residues of partial melting of pelitic red clay[23] (blue squares with cross). (See Supplementary Information for data sources.)

For example, we observe phengite within garnet cores in many of our samples at temperatures $\geq 1,000$ °C, indicating that phengite remained stable up to peak metamorphic conditions—as observed experimentally by Hermann and Green (ref. 21), who report residual phengite at 1,000 °C at 4 and 4.5 GPa, and as in Schmidt *et al.* (ref. 11), who infer that fluid-undersaturated, dehydration melting of phengite occurs from 950 °C at 3 GPa to 1,150 °C at 5 GPa (their Figure 11). We note that some fluid-saturated[22] experiments show lower temperatures for phengite breakdown, however, our results indicate that dehydration melting is a better approximation to the conditions in natural UHP metamorphism.

Our results are consistent with experimental studies of metasediments and metabasalts[12,23,24], which show little depletion

in key trace elements during dehydration melting at 600°–1,000 °C and 2–5 GPa (Fig. 1b–e). The lack of depletion is probably due to the stability of minor phases (for example, phengite, allanite, apatite, monazite, and zircon) that are stable above the fluid-saturated solidus at UHP conditions and retain these key elements[24–26].

Overall, the compiled UHP data imply that recycling of elements such as Th, La, Nd and Pb from metasediments is inefficient if slab-top temperatures are <1,000 °C in the region of arc magma genesis. Although the parameters involved in the mass balance are uncertain, subducting fluxes of Th, U, K, La and Nd, combined with primitive magmatic concentrations of these elements[2] and estimates for magmatic fluxes in arcs, generally yield recycling rates of ~100% (see Supplementary Information for these calculations).
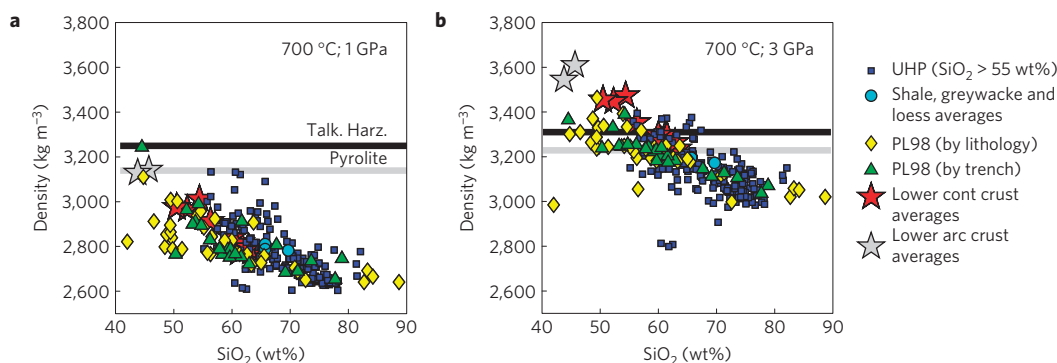
Figure 2 | Density of subducted sediments at UHP conditions. Density calculated at 700 °C and **a**, 1 GPa and **b**, 3 GPa as a function of SiO$_2$ content for compiled UHP metasedimentary compositions (dark blue squares), our estimates of average shale and greywacke, average loess, and the average of prior shale compositional averages (light blue circles), and subducting sediment delineated by lithology (yellow diamonds[30]) and location (green triangles[30]). Average lower continental and arc lower crust[50] are shown with red and grey stars, respectively. Black and grey horizontal lines show densities calculated for harzburgite[14] and pyrolite[35], respectively. Relative to the mantle wedge almost all sediment compositions are buoyant at 700 °C and pressures <3 GPa.

Thus, the apparent efficiency of recycling together with UHP metapelite compositions suggests that the sediment-melt signature in arcs is generated at >1,000 °C—significantly above the fluid-saturated sediment solidus. Temperatures greater than 1,000 °C are not reached on the slab top at pressures less than 5 GPa in even the hottest subduction-zone thermal models. Thus, we argue that the most likely location for the UHP metapelites to have reached temperatures >1,000 °C beneath volcanic arcs is within the mantle wedge. A possible example of this process is recorded by a peraluminous xenolith with oxygen isotopes indicative of a metasedimentary protolith from South Africa, which records peak metamorphic conditions of 1,200–1,300 °C and 4–5 GPa (that is, mantle wedge rather than subduction zone conditions)[27].

Timescale for the formation of sediment diapirs

Numerical modelling studies have shown the potential for subducting sediments to rise buoyantly into the mantle wedge[17,28,29]. However, these studies focused on systems in which the sediments are entrained in buoyant, hydrated mantle diapirs[17,28], or on very thick (>2 km) sediment layers[29], not representative of the thickness of sediment subducting to depth at modern arcs. Moreover, no studies have yet presented formal non-Newtonian scaling for sediment diapirs as a function of such key parameters as sediment thickness and density—preventing quantitative constraints on where and when sediment diapirs may form during subduction. Here we present a new, non-Newtonian scaling analysis for subducting sediments, to assess the timescale and depth at which a sediment layer may become unstable even in the absence of other sources of buoyancy (for example, a hydrated mantle layer).

To evaluate the intrinsic buoyancy of subducting sediments, we first calculated densities for the compiled UHP metapelites and averages of pelitic sediment compositions (ref. 30; Supplementary Information) and compared them to the density of the overlying mantle wedge (see Methods section). At 700 °C and pressures ≤3 GPa, almost all UHP rocks and sediment averages are buoyant with respect to the mantle wedge (Fig. 2). Further, for both warm (Cascadia) and cold (Izu-Bonin) slab-top geotherms[8] the density contrast between the overlying mantle and the average UHP metapelite is as much as −200 kg m^{-3} for all pressures up to 6 GPa (Fig. 3).

The timescale over which instabilities grow in a buoyant sediment layer is related to the relative viscosities of the sediment and overlying mantle, the viscous decay length in the mantle, and the buoyancy and thickness of the sediment layer[31–35]. We calculated instability times assuming a wet olivine rheology for the mantle wedge[36] that is 100× more viscous than the underlying
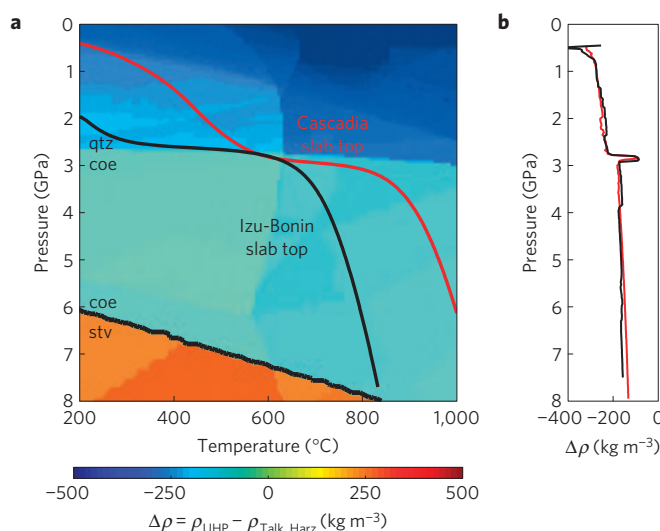

Figure 3 | Density of the average UHP metasediment along typical subduction zone geotherms. a, Density contrast between the average UHP metasedimentary composition and mantle wedge harzburgite[14] as a function of temperature and pressure. Thick red and black lines show slab-top geotherms for Cascadia and Izu-Bonin, respectively[8]. **b**, Density contrast as a function of pressure along the Cascadia (red) and Izu-Bonin (black) slab-top geotherms. Note that the density contrast is ≤ −200 kg m^{-3} for all pressures <6 GPa.

sediment layer (Fig. 4, see Methods section). This viscosity contrast is appropriate for wet quartz[37] at temperatures between 600° and 800 °C. For a 500 m-thick sediment layer with a density contrast of −200 kg m^{-3} relative to the overlying mantle, the timescale for instability formation is <1 Myr and <10 kyr at temperatures of 700 °C and 800 °C, respectively (Fig. 4a and grey region in Fig. 4b). Moreover, any sediment layer thicker than ~100 m will become unstable on timescales shorter than 1 Myr at temperatures ≤1,000 °C (Fig. 4a).

The conditions for diapir formation in a given subduction zone can be determined by integrating the instability time along the slab-top pressure–temperature–time (P–T–t) path until the amplitude of the instability exceeds the initial thickness of the sediment layer. To illustrate this approach, the P–T conditions at which diapirs form in Cascadia and Izu–Bonin were calculated assuming a sediment thickness of 500 m (stars on the black and red curves in Fig. 4b). In both cases, diapirs form between ~675°–750 °C and
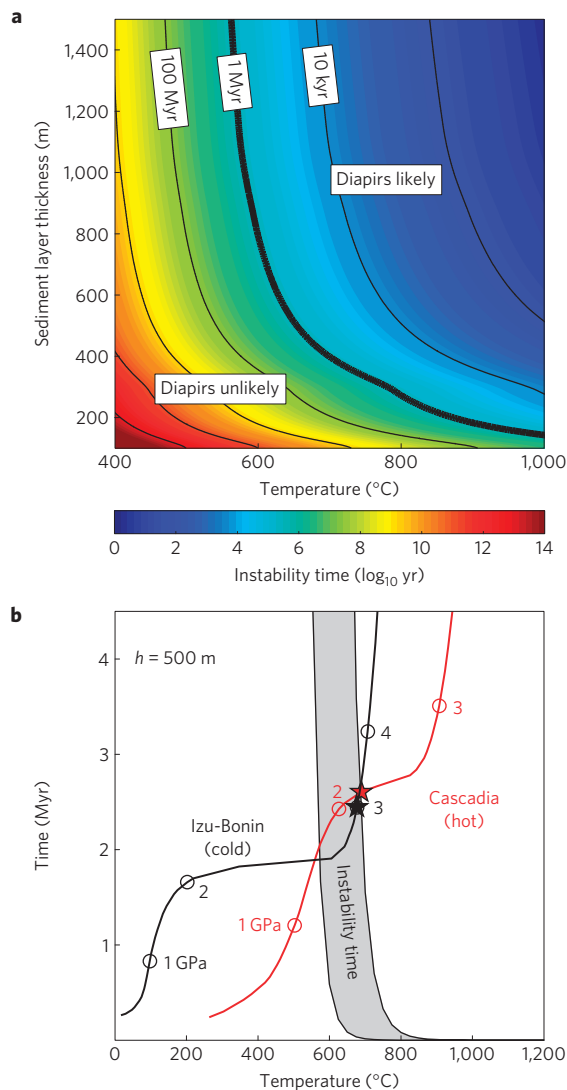
643

Figure 4 | Calculated timescale for the initiation of a sediment diapir.
a, Instability time versus temperature and sediment layer thickness for a density contrast of $-200\,kg\,m^{-3}$, background strain-rate of $10^{-16}\,s^{-1}$, and initial perturbation amplitude 33% of the layer thickness. For typical subduction rates, diapirs form between 2 and 4 GPa if the instability time is $\leq$1 Myr (thick black contour). **b**, Location of diapir formation (stars) on slab-top geotherms for Cascadia (red) and Izu-Bonin (black) assuming a sediment thickness of 500 m. Grey region shows instability times for background strain-rates ranging from 10^{-14} to $10^{-18}\,s^{-1}$. Diapirs are predicted to form at 685 °C and ~2.3 GPa in Cascadia and 730 °C and 3.2 GPa in Izu-Bonin.
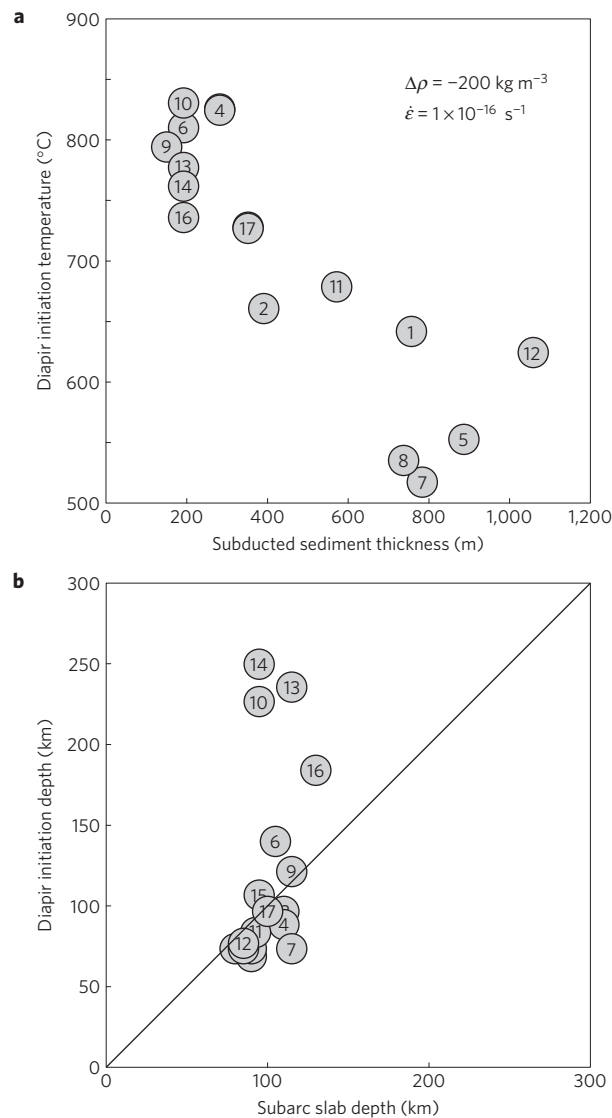

Figure 5 | Summary of conditions for sediment diapir formation in global subduction zones. a, Diapir initiation temperature versus sediment layer thickness[30], and **b**, diapir initiation depth versus subarc slab depth (as compiled in ref. 8) calculated for 17 slab-top geotherms[8]. Subducting sediment layer thicknesses are corrected for compaction to a density of $2,800\,kg\,m^{-3}$. Numbers (in order of increasing slab thermal parameter) correspond to subduction zones: 1—Cascadia, 2—Nankai, 3—Mexico, 4—Colombia-Ecuador, 5—SC Chile, 6—Kyushu, 7—N. Sumatra, 8—Alaska, 9—N. Chile, 10—N. Costa Rica, 11—Aleutians, 12—N. Hikurangi, 13—Mariana, 14—Tonga-Kermadec, 15—Kamchatka, 16—Izu, and 17—NE Japan.

2.2–3.0 GPa, with a slightly greater formation depth in Izu–Bonin due to the colder incoming slab.

Based on slab-top geotherms[8] and the estimated thickness of the downgoing sediment layer[38,39], we explored the conditions of diapir formation for 17 different subduction systems (Fig. 5). For all subduction systems, diapirs form between 500° and 850 °C (Fig. 5a), with higher temperatures corresponding to thinner sediment layers because instability growth rates scale positively with layer thickness[31,34,35]. These temperatures are near the fluid-saturated sediment solidus, but significantly below the ~1,050 °C required to deplete metasediments in Th, Sr, Pb and Nd (Fig. 1). Thus, we conclude that diapirs of buoyant metasediment detach from the downgoing slab and rise buoyantly into the mantle wedge, where they are heated to temperatures >1,000–1,100 °C.

A key difference between these results and previous work is that we predict diapiric rise for sediment layers with wet quartz rheology that are as thin as 100 m, whereas Currie et al. (ref. 29) concluded that buoyant 'wet quartz' layers less than 1-km thick would not form diapirs unless the magnitude of the density contrast was >200 kg m^{-3}. Thus, because the sediment layer thickness is <1 km for all but one of the subduction zones in Fig. 5a, Currie et al.[29] would not predict instabilities for any of these unless the density contrast was consistently significantly greater than 200 kg m^{-3}. Such high density contrasts are inconsistent with our calculated density contrasts for metasediments at UHP conditions (Fig. 2).

Our calculations predict that in all but four subduction zones with very thin sediment layers, diapirs form within ±40 km of

the slab depth below the arc (Fig. 5b). This indicates that partial melts derived from metasedimentary diapirs rising through the hot mantle wedge could easily be incorporated into the arc melting regime. The details of these calculations are sensitive to the slab-top geotherm. Subduction-zone thermal models have evolved considerably over the past 10 years, incorporating effects such as temperature- and stress-dependent rheology, decoupling between the downgoing slab and overriding plate, and variable slab geometry[5–8]. However, many potentially important effects, including thermal advection associated with melts and fluids and thermal/mechanical erosion of the upper plate, have yet to be incorporated into these models. Furthermore, our calculations assume a steady-state thickness of the subducting sediment layer, whereas temporal variations are likely. Thus, although a robust conclusion of our analysis is that diapirs form at temperatures $<\sim850\,^{\circ}$C and near the depth of arc-magma genesis, further details on their formation will require improved subduction-zone thermal models.

Implications for arc volcanism and mantle wedge dynamics

Based on our scaling analysis (see Methods section), diapirs will form from a sediment layer 250–500 m thick with an along-arc spacing of 4–8 km and diameters of 3–4 km. The diffusion time required to raise the temperature to $\geq1,000\,^{\circ}$C at the centre of a sphere with these dimensions is on the order of 10^4 yr assuming that the surrounding mantle is at $1,350\,^{\circ}$C. This is more than an order of magnitude faster than the transit time of a similarly sized diapir through the mantle wedge based on analogue experiments[40], and implies that the sediments would thermally equilibrate and undergo extensive melting before reaching the top of the mantle wedge. However, sediment diapirs of this size would comprise only $\sim0.1\%$ of the mantle wedge by volume, and thus would have a negligible influence on the time-averaged wedge temperature and the kinematics of mantle flow. Furthermore, given their small size they would be difficult to detect seismically. This contrasts with models of buoyant 'cold plumes' that have been proposed to arise from much thicker layers of hydrated mantle located above or below the downgoing plate[17], and/or foundering of dense arc lower crust[41], both of which could significantly alter wedge temperatures and mantle flow patterns. Furthermore, the calculated spacing of sediment diapirs is significantly less than the 30–100 km spacing of most arc volcanoes[32], indicating that the spacing of sediment diapirs is not the underlying cause of the spacing of volcanic centres in arcs.

The high H_2O/Ce and H_2O/K ratios observed in some arcs[11–13] (for example, Tonga, where the rapid convergence rate and great age of the subducting plate combine to yield relatively low slab top temperatures in thermal models) are difficult to explain as the result of extensive melting of metasedimentary diapirs. Instead, it is possible that the subduction component in these arcs is transported from the slab top by means of aqueous fluids or near-solidus, small-degree partial melts, rather than produced by partial melting of diapirs within the mantle wedge. In our study, diapirs are predicted to initiate late, behind the volcanic arc, in the relatively cold Tonga–Kermadec and Mariana–Izu–Bonin arc systems (Fig. 5), where the subducting sediment layer is thin, the recycled sediment signature is muted[2,24], and recycling efficiencies are relatively low (see Supplementary Information).

Finally, the efficient removal and recycling of sediments into the mantle wedge will influence volatile fluxes into the deep mantle at subduction zones. In the case of H_2O, only a small fraction of sediment H_2O ($\sim5\%$) is subducted to postarc depths[42], and thus the formation of sediment diapirs will have a relatively minor influence on the total recycling efficiency. However, decarbonation reactions occur at higher temperatures than dehydration reactions, implying that a greater fraction of carbonate rocks may be transported to postarc depths[43–45]. Currently, global estimates of

the slab-derived CO_2 by decarbonation[43] are significantly less than CO_2 drawdown by silicate weathering[46,47]. Thus, sediment diapirs provide an efficient mechanism for recycling these carbonates into the arc melting regime, and may provide a mechanism to balance the global carbon cycle.

Methods

Sediment densities were calculated using Perple_X 2007 (ref. 48) and thermodynamic data[49] and solution models[42] appropriate for arc mineral assemblages. We assumed 2 wt% H_2O for all compositions, which is representative of the amount of H_2O retained in subducting metasediments at $700\,^{\circ}$C and 3 GPa (ref. 42). Based on the calculated density contrast between the average UHP composition and mantle wedge harzburgite[14] at pressures <4 GPa (Fig. 3b) we assume a value of $-200\,\text{kg m}^{-3}$ for all instability calculations.

The rate of instability growth is sensitive to the viscosity contrast between the buoyant layer and overlying half-space. To determine the viscosity ratio we calculated viscosities for wet quartz[37] and wet olivine[36] ($C_{OH} = 2,500\,\text{H}/10^6$ Si) over a range of temperatures and strain rates. For strain rates of 10^{-16}–$10^{-17}\,\text{s}^{-1}$ (typical of the slab–wedge interface in numerical models of wedge corner flow with non-Newtonian rheology[5,8]), wet olivine is 2–3 orders of magnitude more viscous than wet quartz at 600–800 $^{\circ}$C (the approximate temperature range over which diapirs form). Before 2001, geodynamic studies of density instability assumed that mobile, buoyant crustal layers were more viscous than the adjacent mantle half space, which was then assumed to be inviscid. By contrast, in the scenarios considered here metasediment is much weaker than the mantle. Thus, instability times were calculated based on non-Newtonian growth rates for a 'weak' buoyant layer (layer: half-space viscosity ratio = 1:100) and an assumed background strain rate[35].

Instability growth rates are sensitive to the length-scale over which viscosity decreases in the overlying half-space[31,34]. For wet olivine, a slab-top temperature of $700\,^{\circ}$C, and a vertical temperature gradient of 20–40 $^{\circ}$C km^{-1} across the slab-wedge interface[6], the viscous decay length is ~0.5–1.5 km (ref. 34). The instability growth rates were then calculated based on the ratio of the viscous decay length to the sediment layer thickness[35]. Finally, the spacing of the instabilities was determined from the wavenumber of the fastest growth rate.

References

1. Kessel, R., Schmidt, M. W., Ulmer, P. & Pettke, T. Trace element signature of subduction-zone fluids, melts and supercritical liquids at 120–180 km depth. *Nature* **437,** 724–727 (2005).
2. Plank, T. & Langmuir, C. H. Tracing trace elements from sediment input to volcanic output at subduction zones. *Nature* **362,** 739–743 (1993).
3. Elliott, T., Plank, T., Zindler, A., White, W. & Bourdon, B. Element transport from slab to volcanic front at the Mariana arc. *J. Geophys. Res.* **102,** 14991–15019 (1997).
4. Hawkesworth, C. J., Turner, S. P., McDermott, F., Peate, D. W. & van Calsteren, P. U–Th isotopes in arc magmas: Implications for element transfer from the subducted crust. *Science* **276,** 551–555 (1997).
5. van Keken, P. E., Kiefer, B. & Peacock, S. M. High-resolution models of subduction zones: Implications for mineral dehydration reactions and the transport of water into deep mantle. *Geochem. Geophys. Geosyst.* **3,** 1056 (2002).
6. Kelemen, P. B., Rilling, J. L., Parmentier, E. M., Mehl, L. & Hacker, B. R. in *Inside the Subduction Factory* Vol. 138 (ed. Eiler, J.) 293–311 (Geophysical Monograph, AGU, 2003).
7. Peacock, S. M. *et al.* Thermal structure of the Costa Rica–Nicaragua subduction zone. *Phys. Earth Planet. Inter.* **149,** 187–200 (2005).
8. Wada, I. & Wang, K. Common depth of slab-mantle decoupling: Reconciling diversity and uniformity of subduction zones. *Geochem. Geophys. Geosyst.* **10,** Q10009 (2009).
9. Nichols, G. T., Wyllie, P. J. & Stern, C. R. Subduction zone melting of pelagic sediments constrained by melting experiments. *Nature* **371,** 785–788 (1994).
10. Schmidt, M. W., Vielzeuf, D. & Auzanneau, E. Melting and dissolution of subducting crust at high pressures: The key role of white mica. *Earth Planet. Sci. Lett.* **228,** 65–84 (2004).
11. Plank, T., Cooper, L. B. & Manning, C. E. Emerging geothermometers for estimating slab surface temperatures. *Nature Geosci.* **2,** 611–615 (2009).
12. Hermann, J. & Rubatto, D. Accessory phase control on the trace element signature of sediment melts in subduction zones. *Chem. Geol.* **265,** 512–526 (2009).
13. Hermann, J. & Spandler, C. J. Sediment melts at sub-arc depths: An experimental study. *J. Petrol.* **49,** 717–740 (2008).
14. Kelemen, P. B., Hanghøj, K. & Greene, A. R. in *The Crust* Vol. 3 (ed. Rudnick, R. L.) 593–659 (Treatise on Geochemistry, Elsevier, 2003).
15. Castro, A. & Gerya, T. V. Magmatic implications of mantle wedge plumes: Experimental study. *Lithos* **103,** 138–148 (2008).

645

16. Yin, A. *et al.* Early paleozoic tectonic and thermomechanical evolution of ultrahigh-pressure (UHP) metamorphic rocks in the northern Tibetan plateau, northwest China. *Int. Geol. Rev.* **49,** 681–716 (2007).

17. Gerya, T. V. & Yuen, D. A. Rayleigh–Taylor instabilities from hydration and melting propel 'cold plumes' at subduction zones. *Earth Planet. Sci. Lett.* **212,** 47–62 (2003).

18. Becker, H., Jochum, K. P. & Carlson, R. W. Trace element fractionation during dehydration of eclogites from high-pressure terranes and the implications for element fluxes in subduction zones. *Chem. Geol.* **163,** 65–99 (2000).

19. Bebout, G. E., Ryan, J. G., Leeman, W. P. & Bebout, A. E. Fractionation of trace elements by subduction-zone metamorphism—effect of convergent-margin thermal evolution. *Earth Planet. Sci. Lett.* **171,** 63–81 (1999).

20. Busigny, V., Cartigny, P., Philippot, P., Ader, M. & Javoy, M. Massive recycling of nitrogen and other fluid-mobile elements (K, Rb, Cs, H) in a cold slab environment: Evidence from HP to UHP oceanic metasediments of the Schistes Lustrés nappe (western Alps, Europe). *Earth Planet. Sci. Lett.* **215,** 27–42 (2003).

21. Hermann, J. & Green, D. H. Experimental constraints on high pressure melting in subducted crust. *Earth Planet. Sci. Lett.* **188,** 149–168 (2001).

22. Thomsen, T. B. & Schmidt, M. W. Melting of carbonated pelites at 2.5–5.0 GPa, silicate–carbonatite liquid immiscibility, and potassium–carbon metasomatism of the mantle. *Earth Planet. Sci. Lett.* **267,** 17–31 (2008).

23. Johnson, M. C. & Plank, T. Dehydration and melting experiments constrain the fate of subducted sediments. *Geochem. Geophys. Geosyst.* **1,** 1007 (1999).

24. Klimm, K., Blundy, J. D. & Green, T. H. Trace element partitioning and accessory phase saturation during H_2O-saturated melting of basalt with implications for subduction zone chemical fluxes. *J. Petrol.* **49,** 523–553 (2008).

25. Massonne, H-J., Kennedy, A., Nasdala, L. & Theye, T. Dating of zircon and monazite from diamondiferous quartzofeldspathic rocks of the Saxonian Erzgebirge. *Mineral. Mag.* **71,** 407–425 (2007).

26. Skora, S. & Blundy, J. High-pressure hydrous phase relations of radiolarian clay and implications for the involvement of subducted sediment in arc magmatism. *J. Petrol.* **51,** 2211–2243 (2010).

27. Sharp, Z. D., Essene, E. J. & Smyth, J. R. Ultra-high temperatures from oxygen isotope thermometry of a coesite-sanidine grospydite. *Contrib. Mineral. Petrol.* **122,** 358–370 (1992).

28. Gorczyk, W., Gerya, T. V., Connolly, J. A. D., Yuen, D. A. & Rudolph, M. Large-scale rigid-body rotation in the mantle wedge and its implications for seismic tomography. *Geochem. Geophys. Geosyst.* **7,** Q05018 (2006).

29. Currie, C. A., Beaumont, C. & Huismans, R. S. The fate of subducted sediments: A case for backarc intrusion and underplating. *Geology* **35,** 1111–1114 (2007).

30. Plank, T. & Langmuir, C. H. The chemical composition of subducting sediment and its consequences for the crust and mantle. *Chem. Geol.* **145,** 325–394 (1998).

31. Houseman, G. A. & Molnar, P. Gravitational (Rayleigh–Taylor) instability of a layer with non-linear viscosity and convective thinning of continental lithosphere. *Geophys. J. Int.* **128,** 125–150 (1997).

32. Marsh, B. D. Island arc development: Some observations, experiments, and speculations. *J. Geol.* **87,** 687–713 (1979).

33. Whitehead, J. A. Jr & Luther, D. S. Dynamics of laboratory diapir and plume models. *J. Geophys. Res.* **80,** 705–717 (1975).

34. Conrad, C. P. & Molnar, P. The growth of Rayleigh–Taylor-type instabilities in the lithosphere for various rheological and density structures. *Geophys. J. Int.* **129,** 95–112 (1997).

35. Jull, M. & Kelemen, P. B. On the conditions for lower crustal convective instability. *J. Geophys. Res.* **106,** 6423–6446 (2001).

36. Hirth, G. & Kohlstedt, D. L. in *Inside the Subduction Factory* Vol. 138 (ed. Eiler, J.) 83–105 (Geophysical Monograph, AGU, 2003).

37. Hirth, G., Teyssier, C. & Dunlap, W. J. An evaluation of quartzite flow laws based on comparisons between experimentally and naturally deformed rocks. *Int. J. Earth Sci.* **90,** 77–87 (2001).

38. Clift, P. D. & Vannucchi, P. Controls on tectonic accretion versus erosion in subduction zones: Implications for the origin and recycling of the continental crust. *Rev. Geophys.* **42,** RG2001 (2004).

39. von Huene, R. & Scholl, D. W. Observations at convergent margins concerning sediment subduction, subduction erosion, and the growth of continental crust. *Rev. Geophys.* **29,** 279–316 (1991).

40. Hall, P. S. & Kincaid, C. Diapiric flow at subduction zones: A recipe for rapid transport. *Science* **292,** 2472–2475 (2001).

41. Behn, M. D., Hirth, G. & Kelemen, P. B. Trench-parallel anisotropy produced by foundering of arc lower crust. *Science* **317,** 108–111 (2007).

42. Hacker, B. R. H_2O subduction beyond arcs. *Geochem. Geophys. Geosyst.* **9,** Q03001 (2008).

43. Gorman, P. J., Kerrick, D. M. & Connolly, J. A. D. Modeling open system metamorphic decarbonation of subducting slabs. *Geochem. Geophys. Geosyst.* **7,** Q04007 (2006).

44. Kerrick, D. M. & Connolly, J. A. D. Metamorphic devolatilization of subducted oceanic metabasalts: Implications for seismicity, arc magmatism and volatile recycling. *Earth Planet. Sci. Lett.* **189,** 19–29 (2001).

45. Molina, J. F. & Poli, S. Carbonate stability and fuid composition in subducted oceanic crust: An experimental study on H_2O–CO_2-bearing basalts. *Earth Planet. Sci. Lett.* **176,** 295–310 (2000).

46. Varekamp, J. C. & Thomas, E. Volcanic and anthropogenic contributions to global weathering budgets. *J. Geochem. Expl.* **62,** 149–159 (1998).

47. Berner, R. A. & Kothavala, Z. GEOCARB III: A revised model of atmospheric CO_2 over Phanerozoic time. *Am. J. Sci.* **301,** 182–204 (2001).

48. Connolly, J. A. D. Computation of phase equilibria by linear programming: A tool for geodynamic modeling and its application to subduction zone decarbonation. *Earth Planet. Sci. Lett.* **236,** 524–541 (2005).

49. Holland, T. & Powell, R. Calculation of phase relations involving haplogranitic melts using an internally consistent thermodynamic dataset. *J. Petrol.* **42,** 673–683 (2001).

50. Behn, M. D. & Kelemen, P. B. The relationship between seismic P-wave velocity and the composition of anhydrous igneous and meta-igneous rocks. *Geochem. Geophys. Geosyst.* **4,** 1041 (2003).

Acknowledgements

Author contributions

M.D.B., P.B.K. and G.H. performed the instability calculations. B.R.H., P.B.K. and H-J.M. compiled the UHP metapelite database. P.B.K. compiled the shale and greywacke database and produced the geochemical figures. M.D.B. took the lead in preparing the manuscript with significant input from all authors.

Additional information

Diapirs as the source of the sediment signature in arc lavas

Mark D. Behn, Peter B. Kelemen, Greg Hirth, Bradley R. Hacker, and Hans-Joachim Massonne

Identifying peraluminous UHP metasediments

Supplementary Table 1 presents estimated peak pressure and temperature, and bulk compositions, for UHP metamorphic rocks whose field relations and/or major-element composition indicate a likely protolith of mudstone, shale, greywacke, loess, or pelagic clay. Peak pressures and temperatures were taken from the references indicated; either the PT determination was done on the listed sample or on nearby rocks — see the original references for details. Temperatures accuracies vary from study to study, but are realistically close to ±100°C. The compositions of reported as "BR Hacker, unpublished data" were analyzed at Washington State University using procedures described at http://www.sees.wsu.edu/Geolab/note.html. Newly analyzed samples reported as "HC Massonne, unpublished data" were analyzed by XRF (major elements + Rb, Ba, Sr, Zr, Y, Ni) and ICP-MS (all other trace elements) as described by *Massonne & Czambor* [2007].

In order to identify metasediments we combined two kinds of data. First, many of the felsic rocks in our database were described in field studies as interlayered with marbles, quartzites, and other rocks that clearly have sedimentary protoliths. However, some interlayered felsic rocks could be sills or transposed plutons, and some UHP terrains lack marble and quartzite. Therefore, we also used major-element data projected on ACK and ACF diagrams [*Nesbitt & Young* 1984]. The ACK diagram exploits the fact that most igneous rocks have molar $Al_2O_3 < (CaO+Na_2O+K_2O)$ because feldspars and common ferromagnesian silicates other than garnet have molar $Al_2O_3 < (CaO+Na_2O+K_2O)$. In contrast, weathering preferentially removes $CaO*+Na_2O+K_2O$ (where $CaO*$ is CaO in silicates rather than carbonates and phosphates) and forms rocks that generally are "peraluminous", with molar $Al_2O_3 > (CaO*+Na_2O+K_2O)$. Furthermore, devolatilization of carbonate-bearing sediments could leave excess CaO in UHP metasediments. Similarly, the ACF diagram shows that igneous rocks generally have molar $Al_2O_3 < (CaO + Na_2O + K_2O + FeO* + MnO + MgO)$, where $FeO*$ is all iron considered as FeO, whereas sediments derived from extensive weathering generally have molar $Al_2O_3 > (CaO + Na_2O + K_2O + FeO* + MnO + MgO)$. These relationships can be seen in Supplementary Figure 1. Diagrams in this Figure are made in the spirit of *Nesbitt & Young* [1984], but with some differences. In the ACK diagrams in molar units, A = Al2O3, K = Na2O + K2O, and C = total CaO, not total CaO – (CO2 + P2O5). The CaO concentration in sediments may include some CaO in carbonate and phosphate, and indeed this is why some sediment values in our plots extend toward the C apex. However, in many cases CO2 or P2O5 are not reported in the literature. As can be seen in Supplementary Figure 1-C, we selected UHP metamorphic rocks with A-(C+K) > 0.098 for this study. These correspond to the compositions of peraluminous, or pelitic metasediments.

Comparing peraluminous UHP metasediments to greywacke and shale compositions

Supplementary Tables 2-5 present compiled compositions of fine-grained sedimentary rocks. Supplementary Table 2 is a compilation of individual greywacke and shale sample compositions, Supplementary Table 3 is a compilation of loess compositions, and Supplementary Table 4 is a compilation of previously published average and composite greywacke and shale compositions. Supplementary Table 5 provides a summary of average values. We made these new compilations on the advice of S. McLennan, because we could not find literature values for the variability (e.g., standard deviation) of "average shale". Supplementary Figure 2 illustrates the average and standard deviation for the three different data sets.

Calculating the efficiency of recycling of the subducted sediment component in arc magmatism

Supplementary Table 6 and Supplementary Figure 3 present element recycling efficiencies, in terms of the *arc recycling flux* of a given element (magmatic flux minus mantle derived melt flux) divided by the flux of the same element in subducting sediments. For primitive arc magma compositions, we used regressed arc lava compositions calculated at 6 wt% MgO for the Mexico, Guatemala, Java, the eastern Aleutian oceanic arc, the northern Lesser Antilles, New Hebrides (Vanuatu) and Marianas arcs from *Plank & Langmuir* [1993]. For Aleutian lavas, these values are reported in Supplementary Table 6 and Supplementary Figure 3 as "E(6)", e.g., "Cs(6)". In addition, for the Aleutian island arc we used the data of *Kelemen et al.* [2003a] combined with those of *Singer et al.* [2007]. Values for the eastern Aleutian arc are for volcanoes east of Adak Island and west of the Alaskan continental shelf. Values for the entire arc are for volcanoes west of the Alaskan continental shelf extending to the Komandorsky Islands. To make an approximate correction for the effects of crystal fractionation, we regressed expressions in terms of the natural log of trace element concentration = A + B*molar Mg#, where Mg# = molar MgO/(MgO+FeO*), using data for lavas from the entire arc, as illustrated in Supplementary Figure 4.

The value calculated from the fit at an Mg# of 0.7 (in approximate Fe/Mg exchange equilibrium with mantle olivine) is reported in Supplementary Table 6 and Supplementary Figure 3 as "E(0.7) fit". One can also use the slope of the fit to calculate "fractionation corrected" trace element concentrations in inferred parental melts at Mg# 0.7 for each lava composition. The averages for these are reported as "E(0.7) average", and are 5 to 15% higher than "E(0.7) fit" for each element. Both types of E(0.7) values are significantly lower than the corresponding values at 6 wt% MgO derived by *Plank & Langmuir* [1993] for the eastern Aleutian arc, suggesting to us that the values derived by *Plank & Langmuir* correspond to the composition of magmas that have undergone some fractional crystallization after extraction from the mantle.

In order to remove the flux of elements derived from partial melting of the mantle, we calculated an estimated partial melt of depleted mantle peridotite using values for "depleted" mid-ocean ridge basalts from *Su* [2002] supplemented by values from *Hofmann* [1988], adjusted to yield a concentration of Sm less than or equal to the primitive Aleutian concentration. See Supplementary Table 6 for details of this calculation. This mantle melt composition was subtracted from estimated primitive melts for a given arc.

The concentrations derived by subtracting the mantle melt composition from primitive arc lava compositions were then multiplied by estimated arc magmatic fluxes [*Suyehiro et al.* 1996; *Taira et al.* 1998; *Holbrook et al.* 1999, *Dimalanta et al.* 2002; *Clift & Vannucchi* 2004; *Jicha et al.* 2006] to estimate *arc recycling fluxes* for each element. Fluxes of each element in subducting sediment for each arc were calculated using the data of *Plank & Langmuir* [1998]. The ratio of (arc recycling flux)/(subducting sediment flux) is reported as the "recycling efficiency" in Supplementary Table 6 and Supplementary Figure 3.

These approximate calculations suggest that incompatible trace elements from subducting sediment are efficiently recycled into arc magmas. The ratio of *arc recycling flux* to flux in subducting sediments determined in this way is > 50% for Th, U, K, La, Ce, and Pb in all arcs considered except Tonga.

Our calculations do not account for input of incompatible trace elements from subducting oceanic crust. However, except for Sr, the sediment contribution probably dominates all of the elements whose recycling efficiency is calculated in Supplementary Table 6 [e.g., *Plank*, 2005; *Plank & Langmuir*, 1993]. For example, after accounting for element flux due to partial melting of the mantle wedge, *Class et al.* [2000] estimated that > 97% of recycled light REE and Th in lavas from Okmok and Rechesnoi volcanoes in the Aleutians were derived from subducting sediments, together with >78% of the recycled Pb. By contrast, *Class et al.* estimated that 54 to 80% of the recycled Sr in the same groups of lavas is derived from subducting basalts.

As a result of the high efficiency of recycling of incompatible trace elements from subducting, peraluminous sediments, the residues of the recycling process should display obvious depletion in these elements. As noted in the main body of the text, we do not see systematic depletion of these elements in peraluminous UHP metasediments, compared to shale and greywacke protoliths, until peak temperature exceeds ~ 1050°C. The depletions we observe are most likely caused by dehydration melting of phengite, accompanied by ~ 100% exhaustion of minor phases such as monazite, zircon and allanite, rather than by small degrees of partial melting at the aqueous fluid saturated solidus or subsequent fluid-fluxed melting at temperatures less than 1050°C.

Additional plots of metasedimentary rock compositions versus peak temperature

In Figure 1 in the main body of the paper, we illustrate the fact that systematic depletions of incompatible trace elements, relative to shale and greywacke protoliths, are not

apparent in peraluminous UHP metasediments until peak temperatures exceed ~ 1050°C. In Figure 1, we focus on Th, Sr, Pb and Nd because Th is the quintessential "fluid immobile" element thought to be recycled from subducting sediment into arc magmas, while Sr, Pb and Nd isotopes in many arcs show evidence for recycling of a component from subducting sediment. In Supplementary Figures 5 and 6, we expand upon this observation, adding plots for "fluid mobile" elements, and extending our review to peraluminous high pressure to ultra-high pressure metasediments recording peak temperatures < 700°C. These plots show no significant depletion of peraluminous HP and UHP metasediments in any of these elements at temperatures below ~ 1050°C.

References cited in supplementary text, tables, and figure captions

Barth, M.G., McDonough, W.F., and Rudnick, R.L., 2000, Tracking the budget of Nb and Ta in the continental crust, Chemical Geology 165, 197-213

Beane, R.J., and Sorensen, S.S., 2007, Protolith signatures and element mobility of the Maksyutov complex subducted slab, southern Ural Mountains, Russia: Int. Geol. Review, v. 49, p. 52-72.

Bebout, G.E., J.G. Ryan, W.P. Leeman, and A.E. Bebout, 1999, Fractionation of trace elements by subduction-zone metamorphism - effect of convergent-margin thermal evolution, Earth Planet. Sci. Lett. 171, 63-81.

Busigny, V., Cartigny, P., Philippot, P., Ader, M., and Javoy, M., 2003, Massive recycling of nitrogen and other fluid-mobile elements (K, Rb, Cs, H) in a cold slab environment: Evidence from HP to UHP oceanic metasediments of the Schistes Lustrés nappe (western Alps, Europe): Earth Planet. Sci. Lett., 215, 27-42.

Carswell, D.A., and P. O'Brien, 1993, Thermobarometry and geotectonic significance of high-pressure granulites: Examples from the Moldanubian zone of the Bohemian Massif in Lower Austria, Journal of Petrology, 34, 427-459.

Carswell, D.A., P.J. O'Brien, R.N. Wilson, and M. Zhai, 1997, Thermobarometry of phengite-bearing eclogites in the Dabie Mountains of central China, Journal of Metamorphic Geology 15, 239–252.

Carswell, D.A., 1991, Variscan high P-T metamorphism and uplift history in the Moldanubian Zone of the Bohemian Massif in Lower Austria, European Journal of Mineralogy, 3, 323-342.

Class, C., Miller, D.M., Goldstein, S.L., Langmuir, C.H., 2000, Distinguishing melt and fluid subduction components in Umnak volcanics, Aleutian Arc, G-cubed 1, 1999GC000010

Clift. P., Vannucchi, P., 2004, Controls on tectonic accretion versus erosion in subduction zones: Implications for the origin and recycling of the continental crust, Rev. Geophys. 42, RG2001, 1-31.

Condie, K.C., 1993, Chemical composition and evolution of the upper continental crust: Contrasting results from surface samples and shales: Chem. Geol., v. 104, p. 1-37.

Condie, K.C., 1993, Chemical composition and evolution of the upper continental crust: Contrasting results from surface samples and shales: Chem. Geol., v. 104, p. 1-37.

Cong, B., M. Zhai, T.A. Carswell, R.N. Wilson, Q. Wang, Z. Zhao, and B.F. Windley, 1995, Petrogenesis of ultrahigh-pressure rocks and their country rocks at Shuanghe in Dabieshan, central China, European Journal of Mineralogy, 7, 119–138.

de Sigoyer, J., S. Guillot, J.M. Lardeaux, and G. Mascle, 1997, Glaucophane-bearing eclogites in the Tso Morari dome (eastern Ladakh, NW Himalaya), European Journal of Mineralogy, 9, 1073–1083.

Dimalanta, C., Taira, A., Yumul, G.P. Jr,, Tokuyama, H., Mochizuki, K., 2002, New rates of western Pacific island arc magmatism from seismic and gravity data, Earth Planet. Sci. Lett. 202, 105-115.

Dobretsov, N.L., 1999, Kokchetav Proterozoic microcontinent (1) at Chaglinka artificial lake and UHP of Kumdy-Kol (2-4) and of Chaglinka Village (5), in Field Symposium Guide to the Diamondiferous and High-Pressure Metamorphic Rocks of Kokchetav

Massif (Northern Kazakhstan), edited by N.L. Dobretsov, N.V. Sobolev, and V.S. Shatsky, Novosibirsk.

Fiala, J., Matejovská, and Vanková, 1987, Moldanubian granulites: Source material and petrogenetic considerations, Neues Jahrbuch Fur Mineralogie Abhandlungen, 157, 133-165.

Gaillard, J., Dupre, B., Allegre, C.J., and Negrel, P., 1997, Chemical and physical denudation in the Amazon River Basin: Chem. Geol., v. 142, p. 141-173.

Gallet, S., Jahn, B.-M., and Torii, M., 1996, Geochemical characterization of the Luochuan loess-paleosol sequence, China, and paleoclimatic implications: Chem. Geol., v. 133, p. 67-88.

Gallet, S., Jahn, B.-M., Van Vliet, L.B., Dia, A., and Rossello, E.A., 1998, Loess geochemistry and its implications for particle origin and composition of the upper continental crust: Earth Planet. Sci. Lett., v. 156, p. 157-172.

Gromet, L.P., Dymek, R.F., Haskin, L.A., Korotev, R.L., 1984, The "North American shale composite": Its compilation,major and trace element characteristics, Geochim. Cosmochim. Acta 48, 2469-2482.

Guillot, S., J. de Sigoyer, J.M. Lardeaux, and G. Mascle, 1997, Eclogitic metasediments from the Tso Morari area (Ladakh, Himalaya): evidence for continental subduction during India–Asia convergence, Contributions to Mineralogy and Petrology, 128, 197–212.

Hacker, B.R., P. Luffi, V. Lutkov, V. Minaev, L. Ratschbacher, T. Plank, M. Ducea, A. Patiño-Douce, M. McWilliams, and J. Metcalf, 2005, Near-ultrahigh pressure processing of continental crust: Miocene crustal xenoliths from the Pamir, Journal of Petrology, 46, 1661-1687.

Hacker, B.R., T.B. Andersen, S. Johnston, A.R.C. Kylander-Clark, E. Peterman, E.O. Walsh, and D. Young, 2010, High-temperature deformation during continental-margin subduction & exhumation: The Ultrahigh-Pressure Western Gneiss Region of Norway, Tectonophysics, 480, 149-171.

Hofmann, A.W., 1988, Chemical differentiation of the Earth: The relationship between mantle, continental crust, and oceanic crust, Earth Planet. Sci. Lett. 90, 297-314.

Holbrook, W.S., Lizarralde, D., McGeary, S., Bangs, N., Diebold, J., 1999, Structure and composition of the Aleutian island arc and implications for continental crustal growth, Geology 27, 31-34.

Jahn BM, Gallet S, Han JM, 2001, Geochemistry of the Xining, Xifeng and Jixian sections, Loess Plateau of China: eolian dust provenance and paleosol evolution during the last 140 ka, Chem. Geol. 178, 71-94

Jicha, B.R., Scholl, D.W., Singer, B.S., Yogodzinski, G.M., Kay, S.M., 2006, Revised age of Aleutian island arc formation implies high rate of magma production, Geology 34, 661-664.

Johnston, S.M., H.K. Brueckner, G. Gehrels, C. Manthei, A. Kylander-Clark, and E. Hartz, 2008, Evidence for a Mid-Crustal Continental Suture and Implications for Multistage (U)HP exhumation, Liverpool Land, East Greenland, Eos, Transactions American Geophysical Union, 89, T41B-1964.

Kelemen, P.B., G.M. Yogodzinski and D.W. Scholl, 2003a, Along-strike variation in lavas of the Aleutian island arc: Implications for the genesis of high Mg# andesite and

the continental crust, in Inside the Subduction Factory, AGU Monograph 138, (J. Eiler, ed.), 223-276.

Kelemen, P.B., K. Hanghøj, and A.R. Greene, 2003b, One view of the geochemistry of subduction-related magmatic arcs with an emphasis on primitive andesite and lower crust, in The Crust, (R.L. Rudnick, ed.), Vol. 3, Treatise on Geochemistry, (H.D. Holland and K.K. Turekian, eds.), Elsevier-Pergamon, Oxford, 593-659

Klemd, R., S. Mattes, and M. Okrusch, 1991, High-pressure relics in meta-sediments intercalated with the Weissenstein eclogite, Münchberg gneiss complex, Bavaria, Contributions to Mineralogy and Petrology, 107, 328-342.

Korsakov, A., V.S. Shatsky, N.V. Sobolev, and A.A. Zayachkovsky, 2002, Garnet-biotite-clinozoisite gneiss: a new type of diamondiferous metamorphic rock from the Kokchetav Massif, European Journal of Mineralogy, 14, 915-928.

Korsch, R.J., Roser, B.P., Kamprad, J.L., 1993, Geochemical, petrographic and grain-size variations within single turbidite beds, Sed. Geol. 83, 15-35.

Liu, C.-G., Masuda, A., Okada, A., Yabuki, S., Zhang, J., and Fan, Z.-L., 1993, A geochemical study of loess and desert sand in northern China: Implications for continental crust weathering and composition: Chem. Geol., v. 106, p. 359-374.

Liu, C.-G., Masuda, A., Okada, A., Yabuki, S., Zhang, J., and Fan, Z.-L., 1993, A geochemical study of loess and desert sand in northern China: Implications for continental crust weathering and composition: Chem. Geol., v. 106, p. 359-374.

Massonne, H.-J., 2003, A comparison of the evolution of diamondiferous quartz-rich rocks from the Saxonian Erzgebirge and the Kokchetav Massif: are so-called diamondiferous gneisses magmatic rocks?, Earth and Planetary Science Letters, 216, 347–364.

Massonne, H.J., and A. Czambor, 2007, Geochemical signatures of Variscan eclogites from the Saxonian Erzgebirge, central Europe, Chemie der Erde, 2007, 69-83.

Massonne, H.J., and P.J. O'Brien, 2003, The Bohemian Massif and the NW Himalaya, EMU Notes in Mineralogy, 5, 145-187.

McLennan, S.M., 1981, Trace element geochemistry of sedimentary rocks: Implications for the composition and evolution of the continental crust: PhD Thesis, Canberra, Australian National University.

McLennan, S.M., Taylor, S.R., McCullough, M.T., and Maynard, J.B., 1990, Geochemical and Nd-Sr isotopic composition of deep-sea turbidites: Crustal evolution and plate tectonic associations: Geochim. Cosmochim. Acta, v. 54, p. 2015-2050.

Nesbitt, H.W., and G.M. Young, 1984, Prediction of some weathering trends of plutonic and volcanic rocks based on thermodynamic and kinetic considerations, Geochim. Cosmochim. Acta, 48, 1523-1534.

Nowlan, E.U., H.-P. Schertl, and W. Schreyer, 2000, Garnet–omphacite–phengite thermobarometry of eclogites from the coesite-bearing unit of the southern Dora-Maira Massif, western Alps, Lithos, 52, 197–214.

Plank, T., and C.H. Langmuir, 1998, The chemical composition of subducting sediment and its consequences for the crust and mantle, Chem. Geol., 145, 325-394.

Plank, T., and C.H. Langmuir, 1993, Tracing trace elements from sediment input to volcanic output at subduction zones, Nature, 362, 739-743.

Quinby-Hunt, M.S., Wilde, P., Orth, C.J., and Berry, W.B.N., 1989, Elemental geochemistry of black shales; statistical comparison of low-calcic shales with other shales, in Grauch, R.I., and Leventhal, J.S., eds., Metalliferous Black Shales and Related Ore Deposits, USGS Circular: Washington DC, US Geological Survey, p. 8-15.

Shatsky, V.S., E. Jagoutz, O.A. Kozmenko, V.S. Parkhomenko, M. Troesch, and N. Sobolev, 1999, Geochemistry and age of ultrahigh-pressure rocks from the Kokchetav Massif (northern Kazakhstan), Contributions to Mineralogy and Petrology, 137, 185-205.

Singer, B.S., B.R. Jicha, W.P. Leeman, N.W. Rogers, M.F. Thirlwall, J. Ryan, J. and K.E. Nicolaysen, Along-strike trace element and isotopic variation in Aleutian Island arc basalt: Subduction melts sediments and dehydrates serpentine, J. Geophys. Res. 112, B06206, doi:10.1029/2006JB004897.

Su, Y.J., Mid-ocean ridge basalt trace element systematics: Constraints from database management, ICPMS analyses, global data compilation, and petrologic modeling, PhD thesis, Columbia University, New York, 457 pp.

Suyehiro, K., Takahashi, N., Ariie, Y., Yokoi, Y., Hino, R., Shinohara, M., Kanazawa, T., Hirata, N., Tokuyama, H., Taira, A., 1996, Continental crust, crustal underplating, and low-Q upper mantle beneath an oceanic island arc, Science 272, 390-392.

Taira A, Saito S, Aoike K, Morita S, Tokuyama H, Suyehiro K, Takahashi N, Shinohara M, Kiyokawa S, Naka J, Klaus A, 1998, Nature and growth rate of the northern Izu-Bonin (Ogasawara) arc crust and their implications for continental crust formation, Island Arc 7, 395-407.

Taylor, S.R., and McLennan, S.M., 1985, The Continental Crust: Its Composition and Evolution: Oxford, Blackwell.

Taylor, S.R., McLennan, S.M., and McCullough, M.T., 1983, Geochemistry of loess, continental crust composition and crustal model ages: Geochim. Cosmochim. Acta, v. 47, p. 1897-1905.

Terry, M.P., P. Robinson, and E.J.K. Ravna, 2000, Kyanite eclogite thermobarometry and evidence for thrusting of UHP over HP metamorphic rocks, Nordøyane, Western Gneiss Region, Norway, American Mineralogist, 85, 1637–1650.

Tilton, G.R., W. Schreyer, and H.-P. Schertl, 1991, Pb-Sr-Nd isotopic behavior of deeply subducted crustal rocks from the Dora Maira massif, western Alps, Italy-II: what is the age of the ultrahigh pressure metamorphism, Contributions to Mineralogy and Petrology, 108, 22–33.

Wain, A.L., 1998, Ultrahigh-Pressure Metamorphism in the Western Gneiss Region of Norway, PhD thesis, Oxford University, UK.

Wedepohl, K.H., 1995. The composition of the continental crust, Geochim. Cosmochim. Acta 59, 1217–1232

Willner, A.P., K. Rötzler, and W.V. Maresch, 1997, Pressure-temperature and fluid evolution of quartzo-feldspathic metamorphic rocks with a relic high-pressure, granulite-facies history from the Central Erzgebirge (Saxony, Germany), Journal of Petrology, 38, 307-336.

Zhang, R., T. Hirajima, S. Banno, B. Cong, and J.G. Liou, 1995, Petrology of ultrahigh-pressure rocks from the southern Su-Lu region, eastern China, Journal of Metamorphic Geology, 13, 659-675.

Zhang, Z., Y. Xiao, J. Hoefs, J.G. Liou, and K. Simon, 2006, Ultrahigh pressure metamorphic rocks from the Chinese Continental Scientific Drilling Project: I. Petrology and geochemistry of the main hole (0–2,050 m), Contributions to Mineralogy and Petrology, 152, 421-441.

Supplementary figure captions

Supplementary Figure 1: ACK and ACF diagrams for fine-grained sediments, igneous rocks, and peraluminous UHP metasediments. See text for description of compositional projection procedures for these diagrams. A. Data from our compilation of bulk compositions for shale and greywacke, loess, and average and composite values for greywacke and shale. For data sources, see Supplementary Tables 2, 3 and 4. B. Data from our compilation of arc plutonic rocks [*Kelemen et al.,* 2003b]. C. Data from our compilation of peraluminous UHP metasediments; data sources in Supplementary Table 1. Two apparently incorrect analyses of Ba and Sr concentration, from Tilton et al., 1981, were omitted for clarity.
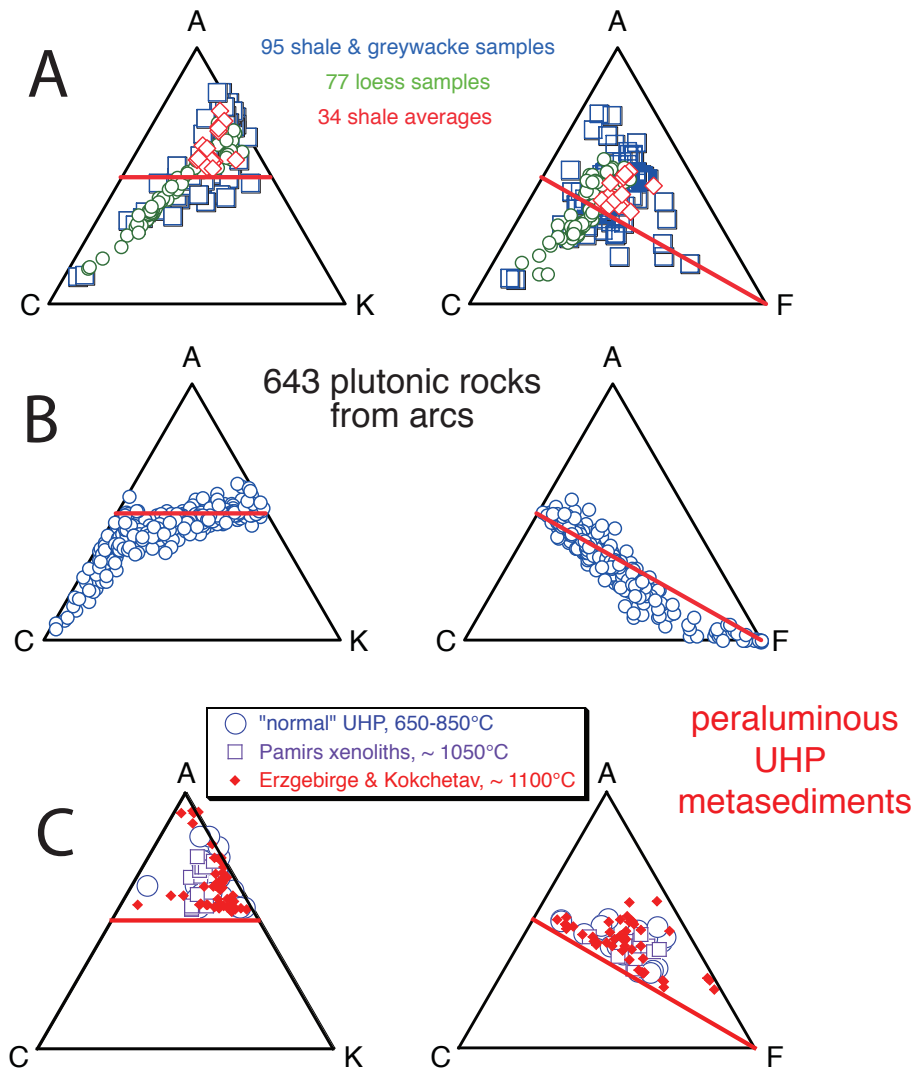
Supplementary Figure 2: Averages +/- 1 standard deviation for greywacke, loess and shale compositions from Supplementary Tables 2, 3 and 4, as summarized in Supplementary Table 5. In some cases, average values – 1 standard deviation were negative. The blue field encloses the average value +/- one standard deviation for at least two of the three data sets, and is used again for comparison to peraluminous UHP metasediment compositions in Figure 1-A in the main body of the paper. Supplementary Table 5 also gives the average and standard deviation for individual samples of *peraluminous* greywacke and shale only, which are used for comparison with UHP compositions in Figures 1-B to 1-E.
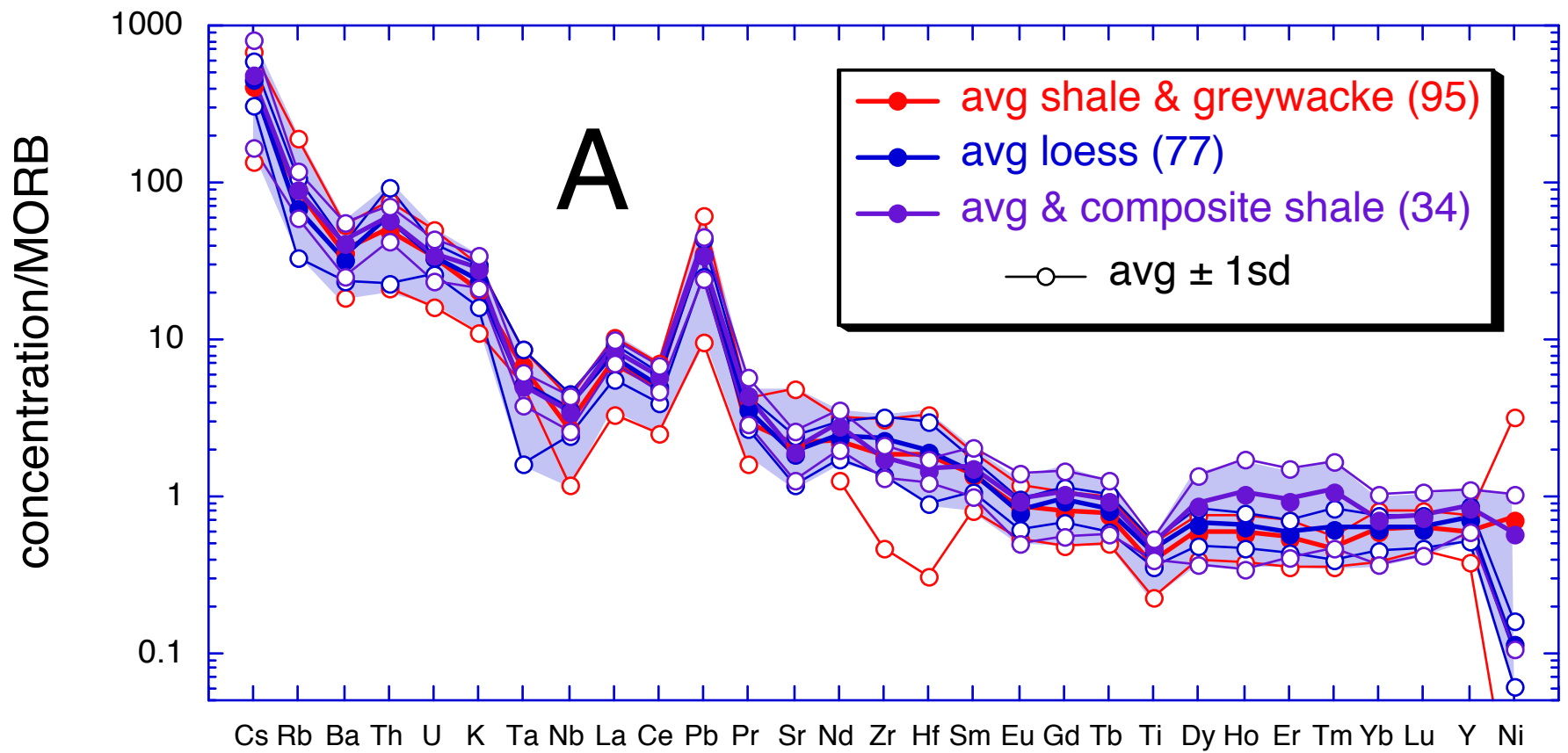
Supplementary Figure 3: Recycling efficiencies (arc recycling flux/sediment flux) for incompatible trace elements in the oceanic Aleutian arc. Sediment fluxes from *Plank & Langmuir* (1993, 1998). Arc magmatic fluxes from *Suyehiro et al.* [1996], *Taira et al.* [1998], *Holbrook et al.* [1999], *Dimalanta et al.* [2002], *Clift & Vannucchi* [2004], and *Jicha et al.* [2006]. Fractionation corrected, primitive magmatic values, mantle-derived melt compositions, sediment fluxes, and resulting recycling efficiencies from Supplementary Table 6.

Supplementary Figure 4: Molar Mg/(Mg+Fe), or Mg#, between 0.15 and 0.75, versus incompatible trace element concentration for lavas from the oceanic Aleutian arc (A & B: west of the continental shelf to the Komandorsky Islands) and for the eastern Aleutian arc (C & D: east of Adak, west of the continental shelf). Data measured and compiled by *Kelemen et al.* [2003] and *Singer et al.* [2007]. Some outliers have been removed for clarity, but the full data set is available in spreadsheet form from Kelemen on request. Fits are in terms of ln(concentration) = A + B•Mg#, or concentration in ppm = A exp (B•Mg#).

Supplementary Figure 5: Temperature versus composition for peraluminous metamorphic rocks in subduction-related settings from Santa Catalina Island [*Bebout et al.* 1999] and the Urals [*Beane & Sorensen* 2007]. As in Figure 1, grey rectangles illustrate the total range of concentrations and the average +/- 1 standard deviation for peraluminous shales and greywackes in Supplementary Table 2, as summarized in Supplementary Table 5.
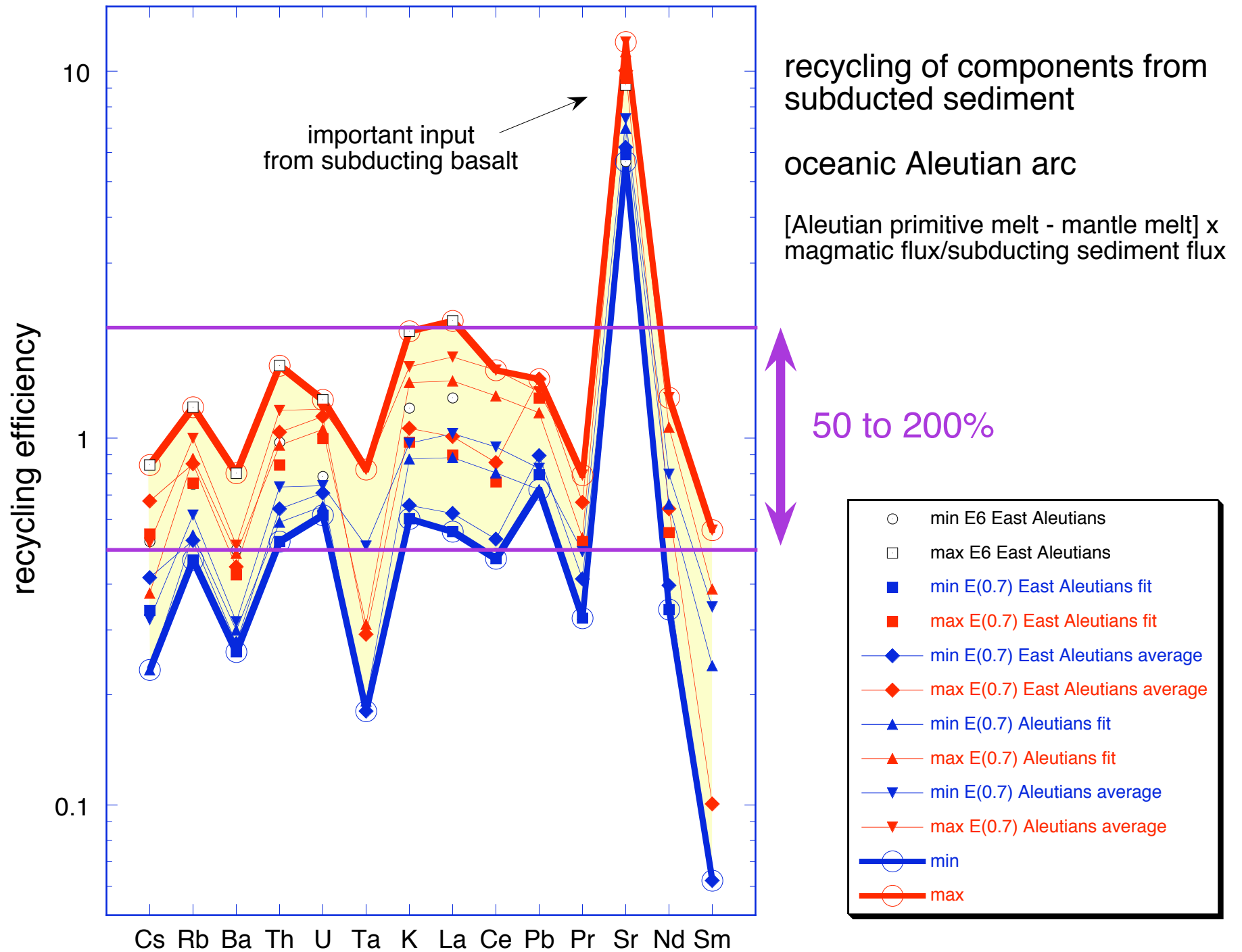
Supplementary Figure 6: Temperature versus composition for peraluminous metamorphic rocks in subduction related settings, and for peraluminous UHP rocks. Data and symbols as for Figure 1 and Supplementary Figure 5, with the addition of data from the western Alps from *Busigny et al.* [2003]. Note that, despite the title referring to "massive recycling of … fluid mobile elements", the *Busigny et al.* data do not show significant depletion compared to peraluminous greywackes and shales, nor do they show systematically decreasing incompatible trace element concentration with increasing temperature.

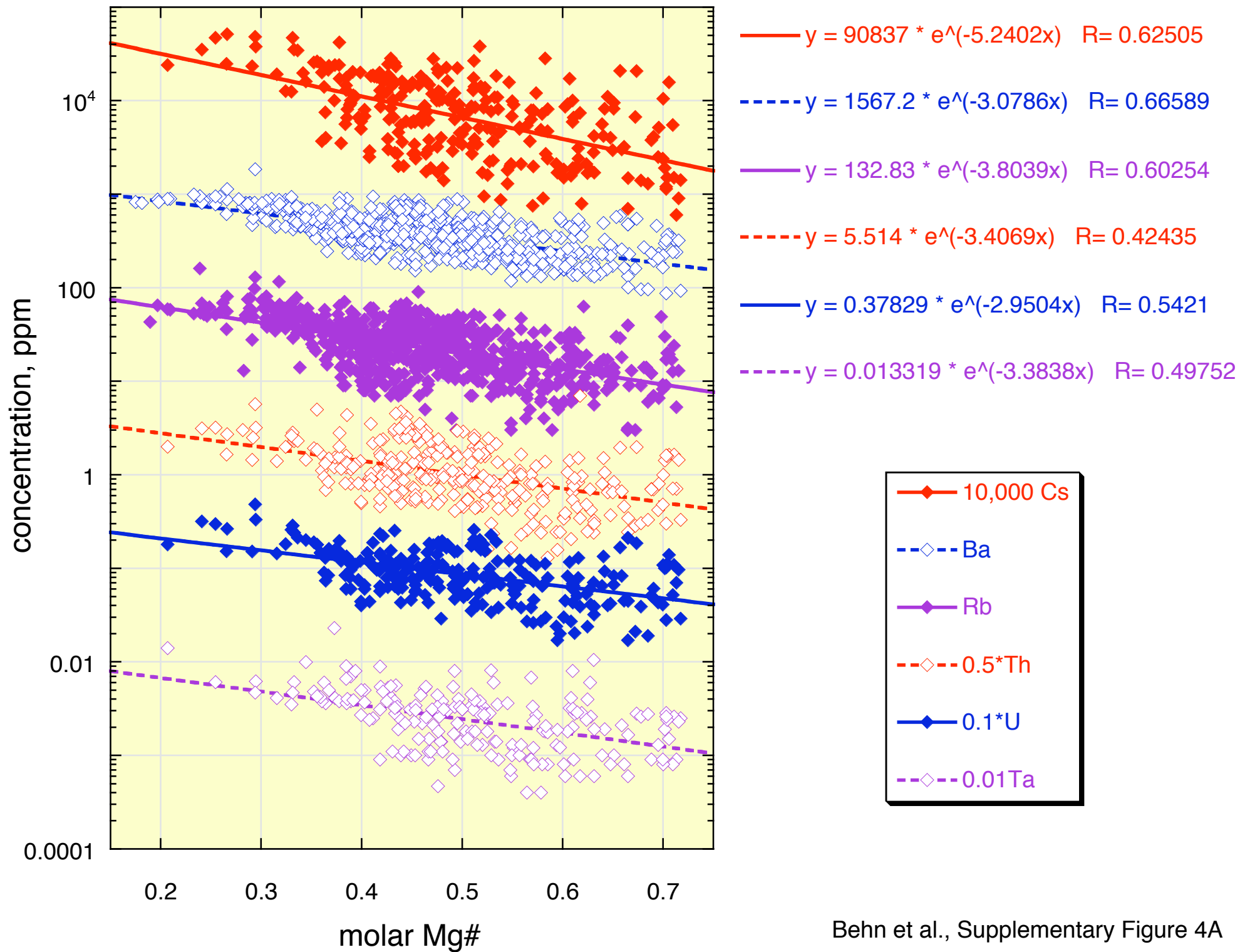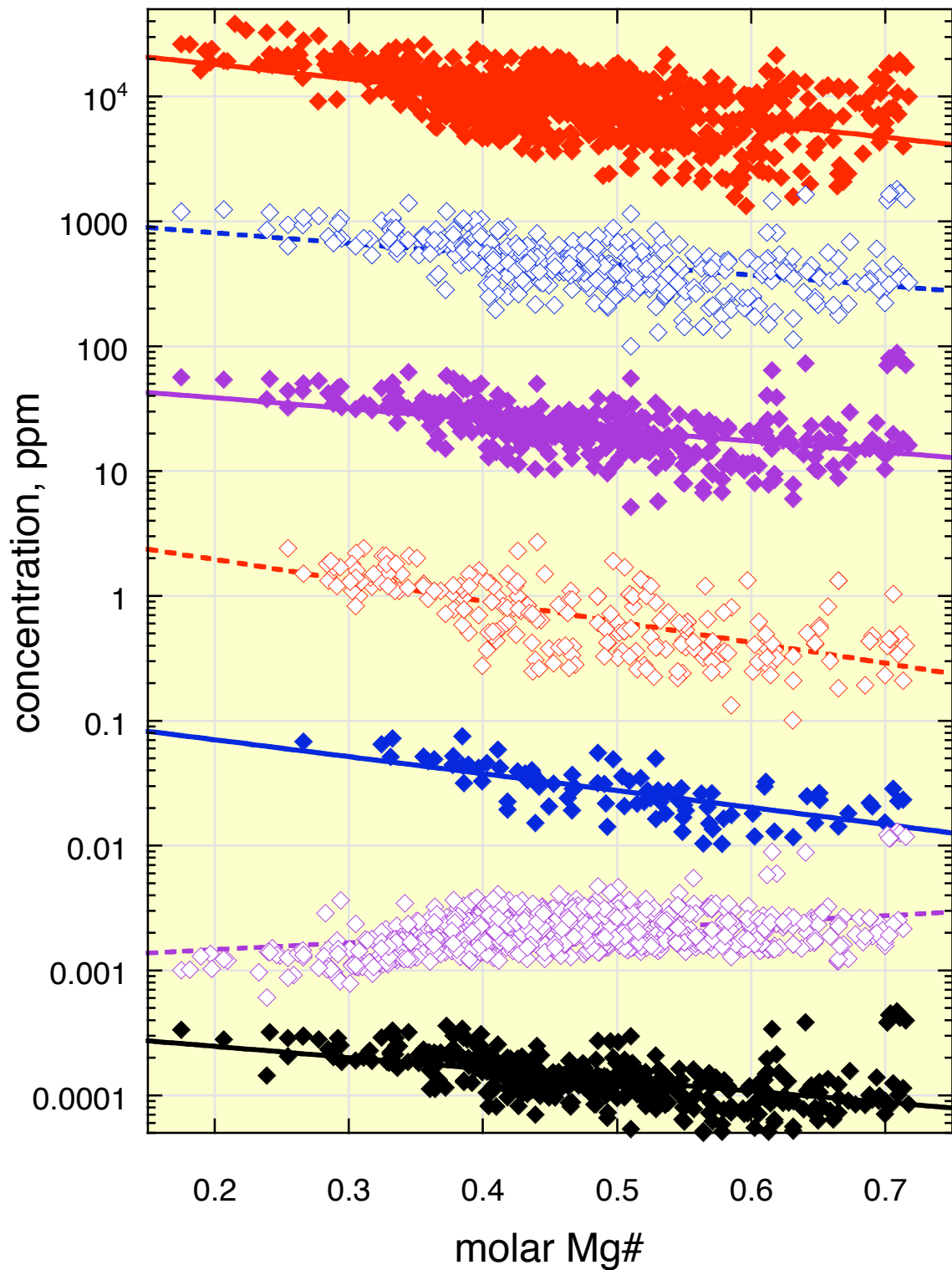**A** — 95 shale & greywacke samples / 77 loess samples / 34 shale averages

B — 643 plutonic rocks from arcs

C — "normal" UHP, 650-850°C / Pamirs xenoliths, ~ 1050°C / Erzgebirge & Kokchetav, ~ 1100°C / peraluminous UHP metasediments

Behn et al., Supplementary Figure 2

recycling of components from subducted sediment

oceanic Aleutian arc

[Aleutian primitive melt - mantle melt] x magmatic flux/subducting sediment flux

important input from subducting basalt

50 to 200%

Legend:
- ○ min E6 East Aleutians
- □ max E6 East Aleutians
- ■ min E(0.7) East Aleutians fit
- ■ max E(0.7) East Aleutians fit
- ◆ min E(0.7) East Aleutians average
- ◆ max E(0.7) East Aleutians average
- ▲ min E(0.7) Aleutians fit
- ▲ max E(0.7) Aleutians fit
- ▼ min E(0.7) Aleutians average
- ▼ max E(0.7) Aleutians average
- min
- max

Behn et al., Supplementary Figure 3

Legend (plotted on chart):

- $y = 90837 * e^{(-5.2402x)}$ R = 0.62505
- $y = 1567.2 * e^{(-3.0786x)}$ R = 0.66589
- $y = 132.83 * e^{(-3.8039x)}$ R = 0.60254
- $y = 5.514 * e^{(-3.4069x)}$ R = 0.42435
- $y = 0.37829 * e^{(-2.9504x)}$ R = 0.5421
- $y = 0.013319 * e^{(-3.3838x)}$ R = 0.49752

Legend:
- 10,000 Cs
- Ba
- Rb
- 0.5*Th
- 0.1*U
- 0.01Ta
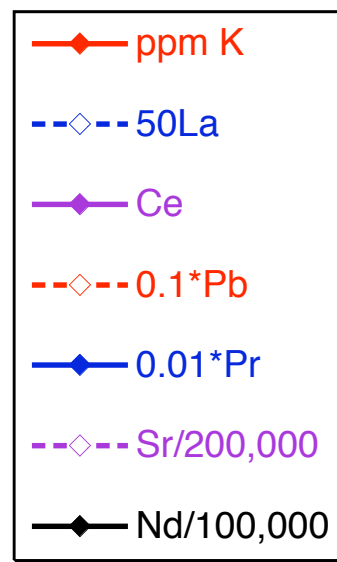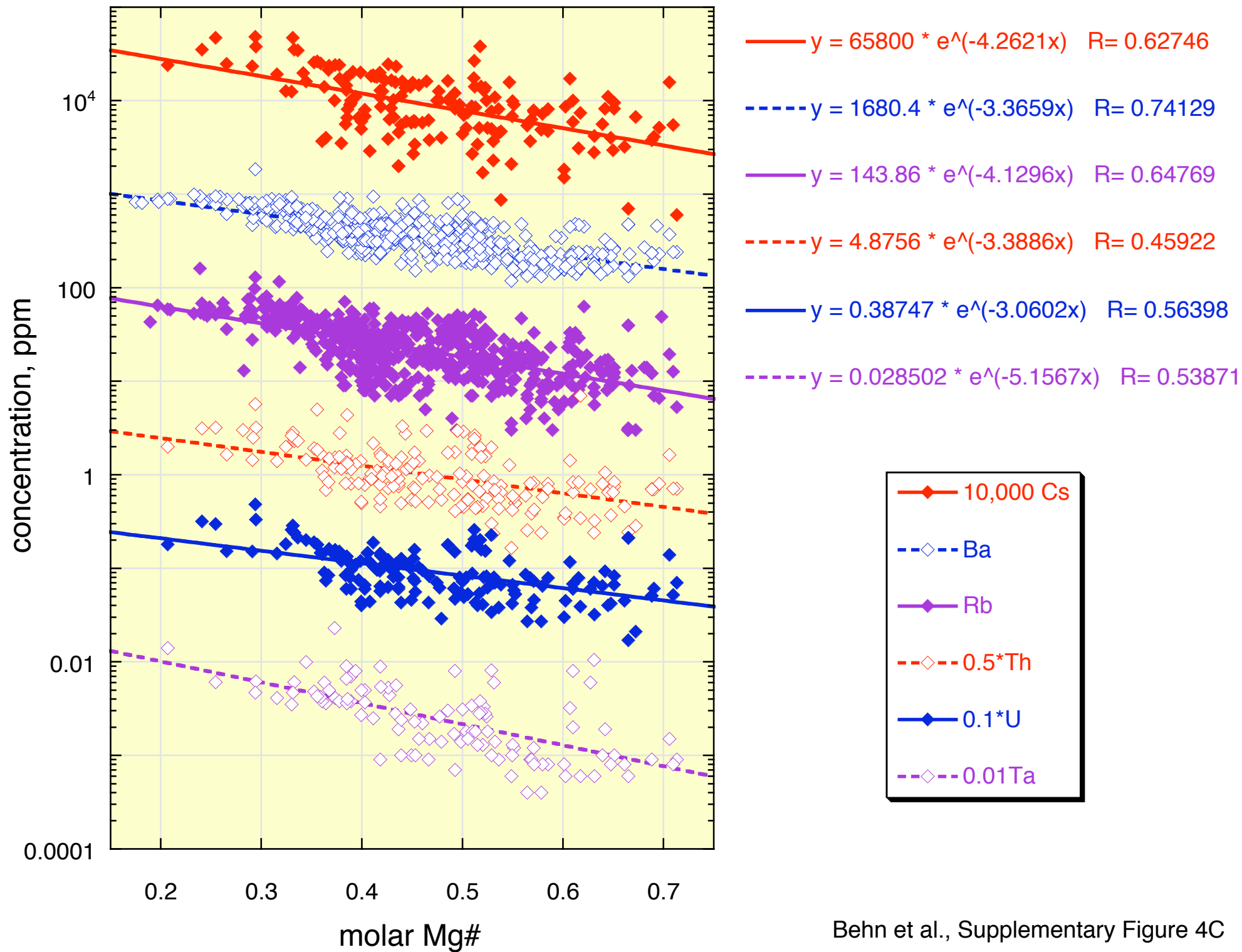
Axis labels: concentration, ppm (y-axis); molar Mg# (x-axis)
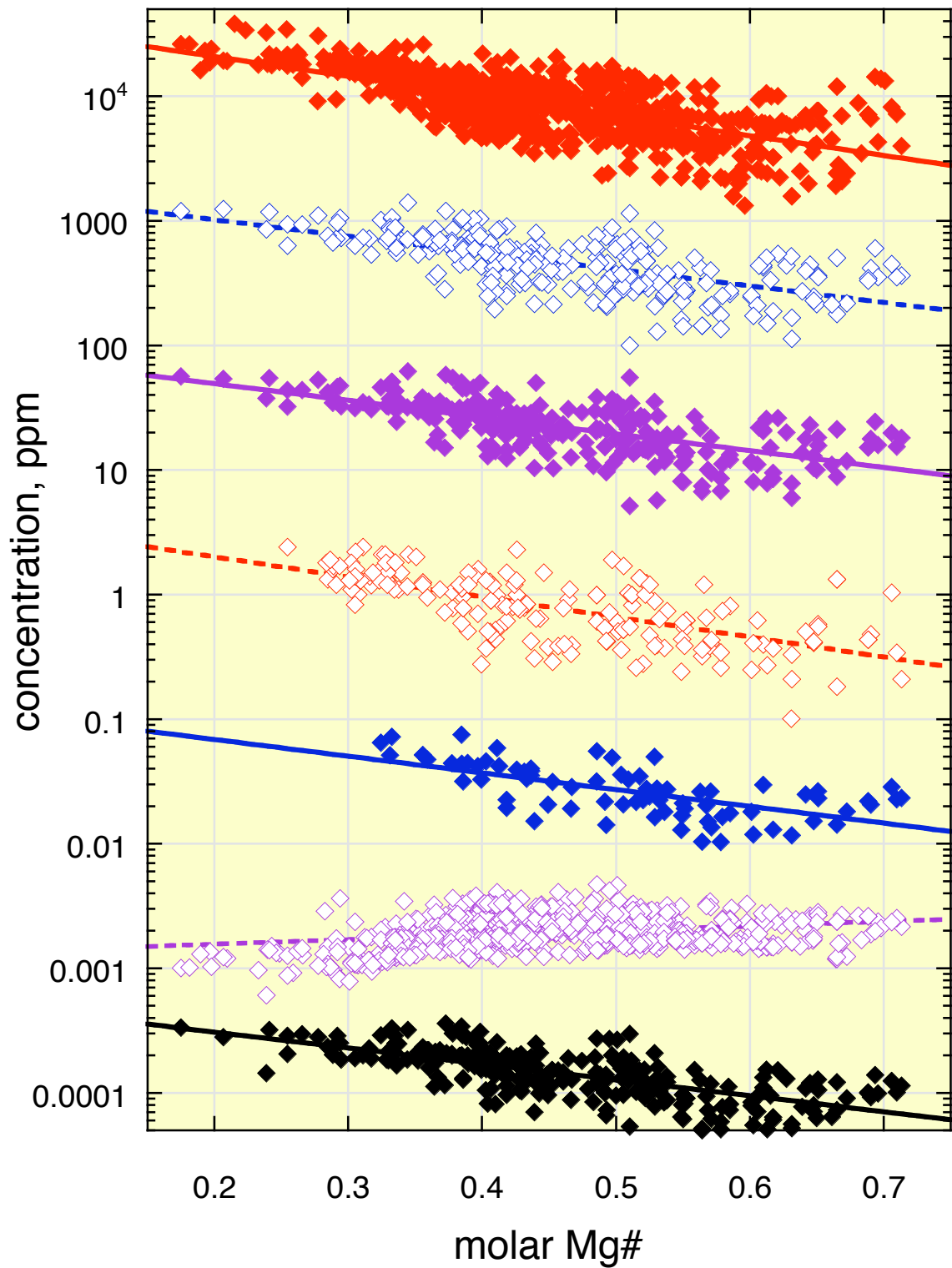
Behn et al., Supplementary Figure 4A

$y = 31110 * e^{-2.6893x}$ R= 0.58146

$y = 1200.8 * e^{-1.95x}$ R= 0.37438

$y = 57.894 * e^{-2.0011x}$ R= 0.38991

$y = 4.2275 * e^{-3.8257x}$ R= 0.69238

$y = 0.13217 * e^{-3.1232x}$ R= 0.75313

$y = 0.0011478 * e^{1.2542x}$ R= 0.32262

$y = 0.00037452 * e^{-2.0641x}$ R= 0.45354

Legend:
- ppm K
- 50La
- Ce
- 0.1*Pb
- 0.01*Pr
- Sr/200,000
- Nd/100,000

concentration, ppm (y-axis)

molar Mg# (x-axis)

Behn et al., Supplementary Figure 4B

$y = 65800 * e^{(-4.2621x)}$ R= 0.62746

$y = 1680.4 * e^{(-3.3659x)}$ R= 0.74129

$y = 143.86 * e^{(-4.1296x)}$ R= 0.64769

$y = 4.8756 * e^{(-3.3886x)}$ R= 0.45922

$y = 0.38747 * e^{(-3.0602x)}$ R= 0.56398

$y = 0.028502 * e^{(-5.1567x)}$ R= 0.53871

10,000 Cs
Ba
Rb
0.5*Th
0.1*U
0.01Ta

Behn et al., Supplementary Figure 4C

Behn et al., Supplementary Figure 4D

Behn et al., Supplementary Figure 5